Phytomedicine 129 (2024) 155685

Contents lists available at ScienceDirect

Phytomedicine

journal homepage: www.elsevier.com/locate/phymed

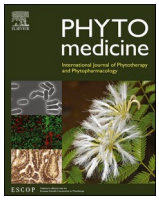

Original Article

Unveiling the metabolites underlying the skin anti-ageing properties of *Cytinus hypocistis* (L.) L. through a biochemometric approach

Ana Rita Silva [a,b,c,d,*], Manuel Ayuso [a,b], Pablo A. García [c], Lillian Barros [a,b], RuAngelie Edrada-Ebel [d,*]

[a] Centro de Investigação de Montanha (CIMO), Instituto Politécnico de Bragança, Campus de Santa Apolónia, 5300-253 Bragança, Portugal
[b] Laboratório Associado para a Sustentabilidade e Tecnologia em Regiões de Montanha (SusTEC), Instituto Politécnico de Bragança, Campus de Santa Apolónia, 5300-253 Bragança, Portugal
[c] Departamento de Ciencias Farmacéuticas. Facultad de Farmacia, CIETUS-IBSAL, Universidad de Salamanca, 37007 Salamanca, España
[d] Strathclyde Institute of Pharmacy and Biomedical Sciences, University of Strathclyde, The John Arbuthnott Building, 161 Cathedral Street, Glasgow G4 0RE, United Kingdom

ARTICLE INFO

Keywords:
Metabolomics
Multivariate statistical analysis
Neutrophil elastase
ellagitannins

ABSTRACT

Background: The genus *Cytinus*, recognised as one of the most enigmatic in the plant kingdom, has garnered attention for its bioactive potential, particularly its skin anti-ageing properties. Despite this recognition, much remains to be accomplished regarding deciphering and isolating its most active compounds.
Hypothesis: This study aimed to identify the compounds responsible for *C. hypocistis* skin anti-ageing potential.
Methods: Using multivariate analysis, a biochemometric approach was applied to identify the discriminant metabolites by integrating extracts' chemical profile (Liquid Chromatography–High-Resolution Mass Spectrometry, LC—HRMS) and bioactive properties. The identified bioactive metabolite was structurally elucidated by 1D and 2D Nuclear Magnetic Resonance (NMR).
Results: Among the studied bioactivities, the anti-elastase results exhibited a significant variation among the samples from different years. After the biochemometric analysis, the compound 2,3:4,6-bis(hexahydroxydiphenoyl)glucose, with a molecular mass of 784.075 Da, was structurally elucidated as the discriminant feature responsible for the outstanding human neutrophil elastase inhibition. Remarkably, the subfraction containing this compound exhibited a tenfold improvement in neutrophil elastase inhibition efficacy compared to the crude extract; its effectiveness fell within the same range as SPCK, a potent irreversible neutrophil elastase inhibitor. Moreover, this subfraction displayed no cytotoxicity or phototoxicity and excellent efficacy for the tested anti-ageing properties.
Conclusions: Hydrolysable tannins were confirmed as the metabolites behind *C. hypocistis* skin anti-ageing properties, effectively mitigating critical molecular mechanisms that influence the phenotypically distinct ageing clinical manifestations. Pedunculagin was particularly effective in inhibiting neutrophil elastase, considered one of the most destructive enzymes in skin ageing.

Introduction

Plants are one of the oldest forms of healthcare known to humankind. Despite being used as medicine since ancient times, from a plant physiology and biochemistry perspective, there are still numerous opportunities for research on its phytomedicinal properties (Veiga et al., 2020).

Nevertheless, the interactions among the numerous constituents present in plant extracts, whether synergistic, additive/non-interactive, or antagonistic, often complicate the determination of the identified properties (Enke and Nagels, 2011). Despite the challenge, most research methodologies employed in investigating botanical mixtures tend to adopt a reductionist approach, primarily focusing on a few specific compounds or disregarding extracts' chemical composition altogether (Caesar and Cech, 2019). These restrictive methodologies, combined with compositional variability of plant extracts - resulting from the environment and genetics factors and the processing techniques applied to the raw material - make it difficult to identify bioactive

* Corresponding authors.
E-mail addresses: anasilva@ipb.pt (A.R. Silva), ruangelie.edrada-ebel@strath.ac.uk (R. Edrada-Ebel).

https://doi.org/10.1016/j.phymed.2024.155685
Received 24 November 2023; Received in revised form 1 March 2024; Accepted 24 April 2024
Available online 26 April 2024

compounds in complex mixtures, elevating the safety risk associated with their use (Rahman et al., 2019).

Bioassay-guided fractionation is a highly effective method used to investigate plant drugs. It involves separating active extracts using various chromatographic techniques to uncover the bioactive components of complex mixtures (Mani et al., 2022). Dereplication protocols quickly identify compounds by comparing spectral signatures with natural product databases or open-source cheminformatic tools (Najmi et al., 2022). However, bioassay-guided fractionation prioritises isolating compounds most easily separated in the mixture rather than targeting those most likely to be active (Kellogg et al., 2016). Therefore, researchers have effectively explored a methodology known as 'biochemometrics,' which employs multivariate statistics on combined chemical and biological datasets obtained during fractionation, regardless of their respective concentrations (Caesar and Cech, 2019).

The health benefits of phenolic compounds extend to preventing and mitigating specific skin disorders (Działo et al., 2016). Unlike other organs that do not always show the obvious structural signs of ageing, the skin regularly exhibits the effects of time resulting from intrinsic and extrinsic factors. Extrinsic ageing is often synonymous with photo-ageing since UVR is its primary contributor, accounting for 80 % of the visible signs (Flament et al., 2013; Russell-Goldman and Murphy, 2020). Despite the skin's effective barrier function, UVR induces oxidative stress, activating pathways leading to the degradation of essential extracellular matrix proteins through the upregulation of metalloproteinases (MMPs) and other enzymes (MacDonald-Wicks et al., 2006; Pittayapruek et al., 2016). Neutrophil elastase, which is known for its destructive potential, not only disrupts MMPs but also has a direct and significant impact on multiple processes, including skin ageing, cancer, psoriasis, scleroderma, bronchiectasis, and cystic fibrosis. Therefore, searching for novel neutrophil elastase inhibitors holds promise across diverse medical disciplines (Lerman and Hammes, 2018; Nunes et al., 2020; Voynow and Shinbashi, 2021).

While recent studies have elucidated the potential of *C. hypocistis* extracts as a valuable source of bioactive compounds with skin anti-ageing properties, including antioxidant, anti-inflammatory, antibacterial, and enzyme-inhibitory activities, their active constituents remain undisclosed (Sanjust and Rinaldi, 2021; Silva et al., 2020). Therefore, this study aimed to identify the compounds responsible for the skin anti-ageing potential of *Cytinus hypocistis* (L.) L. subsp. *macranthus* Wettst. A biochemometric approach was applied to determine the discriminant metabolites associated with its most relevant bioactive properties using LC—HRMS, multivariate statistical analysis, and structural elucidation by 1D and 2D (NMR).

Material and methods

Plant collection

The parasitic species *C. hypocistis* (**Figure S1**) was collected for three

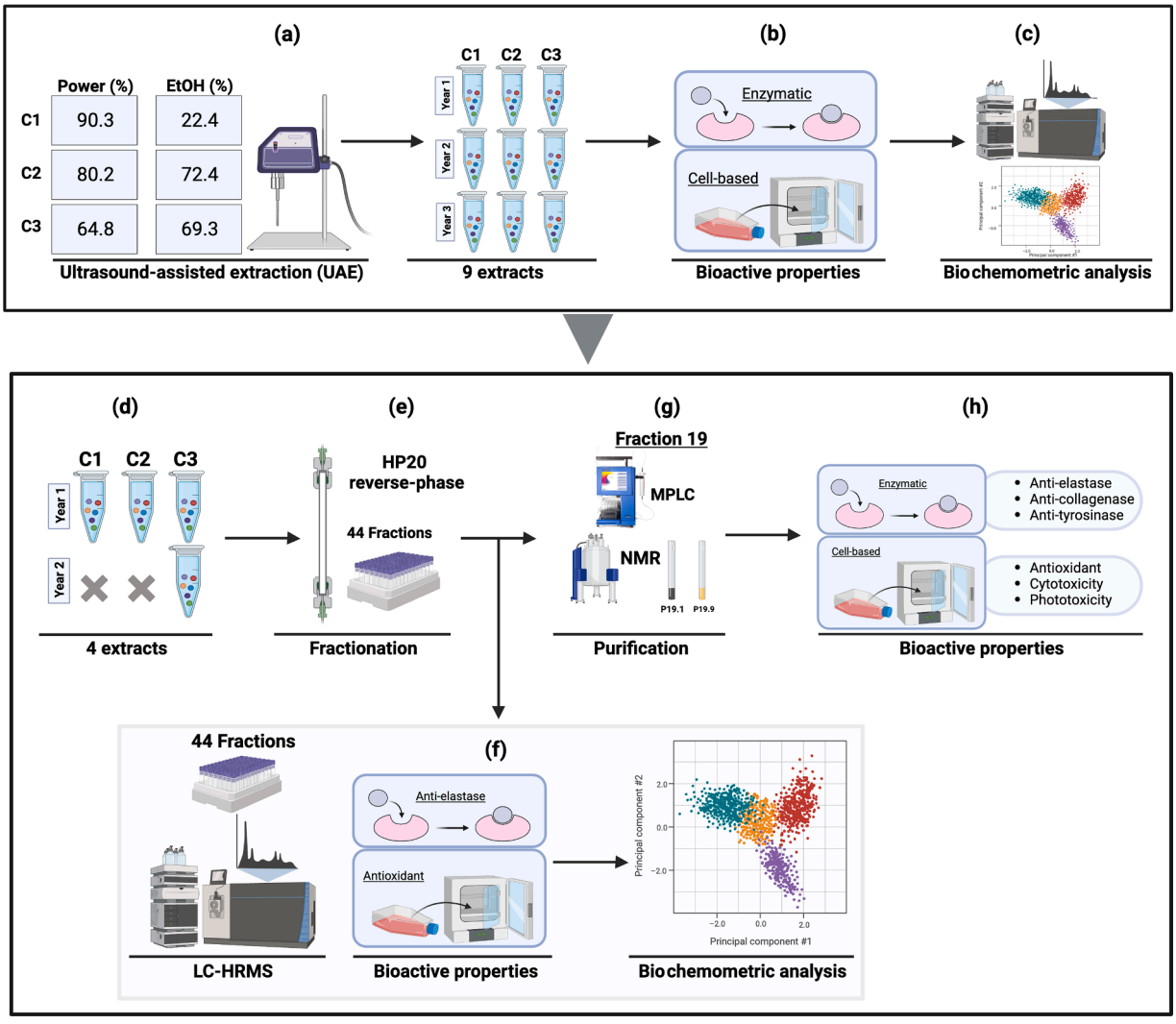

Fig. 1. Schematic representation of the conducted experimental design.

consecutive years (2018–2020) in a shrubland located in Castro Daire, Portugal (40°57′51.0″N 7°51′03.2″W) on the same calendar date in July. As per the data from the Portuguese Institute for Sea and Atmosphere (**Table S1**), the following average minimum and maximum temperatures and precipitation levels were obtained from May to July in the collection years. In 2018, the mean minimum temperature, maximum temperature, and precipitation were 11.3 °C, 22.7 °C, and 44.2 ppm, respectively. In 2019, these values were 11.0 °C, 23.8 °C, and 21.3 ppm, and in 2020, they were 13.3 °C, 26.1 °C, and 22.5 ppm. Appropriate plant preparation was conducted as previously described (Silva et al., 2019), and plant identification was confirmed by Doctor Carlos Aguiar, a botanist from the Polytechnic Institute of Bragança (Portugal).

Biochemometric approach

Fig. 1 illustrates a schematic representation of the experimental design conducted in the present study. Nine extracts (3 extraction conditions C1/C2/C3×3 years) were prepared using ultrasound-assisted extraction **(a)** following the optimum variables previously published (Silva et al., 2021). These samples were assayed for their bioactive properties **(b)**. A biochemometric evaluation was conducted by integrating extracts' chemical (LC—HRMS) and most relevant bioactive (anti-elastase) profiles **(c)**. Based on this analysis, fractionation of the most promising anti-elastase extracts **(d)** using an HP20 reverse-phase column **(e)** was performed. Concurrently, extracts yielding the least favourable anti-elastase results were also fractionated to validate the putative discriminating features. After fractionation, a comprehensive analysis of fractions obtained was conducted using LC—HRMS, along with evaluations of their anti-elastase and antioxidant activities, followed by multivariate analysis to integrate the data **(f)**. Finally, fraction 19 was selected for subsequent purification through medium-pressure liquid chromatography (MPLC) **(g)**. The subfractions obtained (P19.1 and P19.9) underwent assessments for their bioactive properties **(h)** and NMR elucidation. The preparation of the crude extracts, fractions, and subfractions is detailed in the **supplementary material**.

Skin anti-ageing properties

The safety of the tested samples was thoroughly assessed by conducting both cytotoxic and phototoxic evaluations. Their efficacies were investigated through cell-based and enzyme-inhibitory assays. The tested concentrations were chosen based on the IC_{50} range determined in preliminary tests (data not shown) and maintained below the IC_{50} values observed for the cytotoxicity tests. Cell culture conditions are detailed in the **supplementary material**.

Cytotoxic activity. The cell density determination following incubation with *C. hypocistis* extracts and subfractions was conducted using an adapted protocol based on the sulforhodamine B method described by Magalhães and colleagues (Guimarães et al., 2013). HFF-1 and HaCaT cells were plated (90 µl) at an appropriate density (2.0×10^4 cells/well) in a 96-well optical-bottom to adhere overnight. Afterwards, 10 µl (at least $n = 6$) of different extracts (400, 200, 100, 50, 25, 12.5 µg/ml) or subfractions (200, 100, 50, 25 µg/ml) concentrations were added and incubated for 48 h. The ethanol (EtOH) or methanol (MeOH) solvent concentration per well was maintained across all tested samples (1 %). Ten µl of media with 1 % solvent concentration was used as a negative control, considered 100 % viable against which sample-treated cells were compared. ECOSURF™ EH-9 (2 %; A9778, Panreac) was used as a positive control (0 % viability). Cells were then fixed by adding a cold 10 % trichloroacetic acid solution (50 µl) and incubated for 60 min at 4 ºC. Plates were washed three times with deionised water, dried, and incubated with a sulforhodamine B (Sigma; S1402) solution (SRB, 0.1 % in 1 % acetic acid, 100 µl) for 30 min at room temperature. Unbound SRB was washed three times with a 1 % acetic acid solution. Finally, the plates were air-dried, the attached SRB solubilised with 200 µl of 10 mM Tris, and the absorbance was measured at 565 nm using the SPECTROstar Nano Multi-Detection Microplate Reader (BMG Labtech, Ortenberg, Germany). All results were confirmed microscopically. The data were analysed using Graph Pad Prism Software (Graph Pad Prism version 10.0.2 for Windows, GraphPad Software, La Jolla, CA, USA). The results were expressed as sample concentration required to inhibit a 50 % cell viability, IC_{50} mean ± SEM.

3T3 Neutral Red Uptake (NRU) phototoxicity activity. The 3T3 neutral red uptake phototoxicity determination followed the OECD TG 432 (Test No. 432: In vitro 3T3 NRU Phototoxicity Test) (*Test No. 432: In Vitro 3T3 NRU Phototoxicity Test*, 2019). BALB/3T3 cells were plated (100 µl DMEM) at an appropriate density (1.0×10^4 cells/well) in two 96-well optical-bottom plates and incubated overnight. Extracts and subfractions serial dilutions were prepared in Hank's Balanced Salt Solution (HBSS; Corning; 21–023-CV) at the same concentrations described for the cytotoxicity assay. Chlorpromazine (Sigma; C8138), a known phototoxic substance, was used as a positive control. Previously to irradiation, cells were washed with HBSS and then incubated with 10 µl of each sample (at least $n = 6$; final solvent concentration of 1 % EtOH or MeOH) and 90 µl of HBSS. HBSS with 1 % solvent was used as a negative control and considered 100 % viable against which sample-treated cells were compared. Thereafter, one plate was exposed to a non-cytotoxic irradiation dose (5 J/cm^2 as required in the OECD guideline) using an irradiation chamber (JP Selecta, Barcelona, Spain), whereas the other plate was kept in the dark. Following irradiation, cells were gently washed twice with HBSS and incubated for 24 h in a free-serum DMEM media for both treatments. The plates were then rewashed and incubated for 3 h with neutral red (Sigma N4638; 50 µg/ml in free-serum DMEM). Hereafter, 150 µl of solubilising solution (50 ethanol:1 acetic acid:49 ultrapure water) was added to all wells and shaken for 20 min, followed by absorbance measurement at 540 nm. The Phototox version 2.0 software (OECD) was used to calculate the photo irritation factor (PIF), mean photo effect (MPE), and concentration that inhibited cell growth in 50 % compared to untreated cells (IC_{50}). According to these parameters, samples can be classified as non-phototoxic (PIF < 2 or MPE < 0.1), probably phototoxic ($2 <$ PIF < 5 or $0.1 <$ MPE < 0.15), or phototoxic (PIF > 5 or MPE > 0.15).

Cellular antioxidant activity (CAA). The intracellular antioxidant capacity of *C. hypocistis* extracts, fractions, and subfractions was assessed in HFF-1 and HaCaT cell lines using the CAA method described by Liao and colleagues, with some modifications (Liao et al., 2014). A cell suspension was plated (100 µl/well in DMEM) at an appropriate density (3.0×10^4 cells/well) in 96 flat-bottom black background plates to adhere overnight. Samples serial dilutions were prepared to have 6 points of concentration in µg/ml for each extract (200, 100, 50, 25, 12.5, 6.25), and 5 points for each fraction (100, 50, 25, 12.5, 6.25) and subfraction (60, 30, 15, 6.25, 3.75). Ascorbic acid was used as a positive control, and DMEM-free serum media containing 1 % samples' solvent was used as a negative control (Basal reactive oxygen species formation, ROS). Before ROS detection, each well was washed with HBSS and incubated for 3 h with 20 µl of samples/positive control and 180 µl of the DCFH-DA fluorescent redox probe (2′,7′-Dichlorodihydrofluorescein diacetate; 27.8 µM) dissolved in DMEM-free serum media. Post incubation, each well was washed with HBSS and 100 µl of a 2,2′-azo-bis-2-methyl-propanimidamide dihydrochloride solution (AAPH; 600 µM) dissolved in HBSS was added to each well, except for the negative control (100 µl HBSS). The plates were immediately placed on a microplate reader (FLX800 Biotek), where the fluorescence produced by the ROS oxidation of DCFH-DA was read every 10 min for 1 h at an excitation wavelength of 485 nm and an emission wavelength of 538 nm. The percentage inhibition of the tested samples was calculated using the slope from the kinetic curve that presented a better fit for the data. Then, these percentages were plotted against their concentrations to determine the required sample concentration to inhibit 50 % ROS formation (IC_{50}). The data were analysed using Graph Pad Prism Software, and the results were expressed as IC_{50} mean ± SEM.

Anti-collagenase activity. The capacity of the tested extracts and

subfractions to inhibit collagenase activity was analysed using the fluorometric Collagenase Inhibitor Screening Kit (Abcam; ab211108). Briefly, the collagenase substrate was reconstituted with 210 µl of collagenase assay buffer (CAB) and diluted (1:50 µl). A known collagenase inhibitor (1,10)-Phenanthroline (800, 160, 32 µM), was used as the positive control (PCC). Samples were prepared to have 3 points of concentration in µg/ml for each extract (400, 200, 100) and 4 points for each subfraction (30, 15, 7.5, 3.75). The reaction wells were prepared according to the manufacturer's instructions: (samples) 1 µl sample + 5 µl collagenase + 44 µl CAB; (PCC) 1 µl inhibitor + 5 µl collagenase + 44 µl CAB; (enzyme control) 5 µl collagenase + 45 µl CAB; and (background control) 50 µl CAB. The components were mixed in a 96-white opaque plate and incubated for 15 min at room temperature. Finally, 50 µl of reaction mix (48 µl CAB + 2 µl collagenase substrate) was added to each well. The relative fluorescence units (RFU) were measured at 37ºC with an excitation wavelength of 490 nm and an emission of 520 nm using a microplate reader (FLX800 Biotek) in kinetic mode (30–60 min). The percentage inhibition of the tested samples was calculated using the slope from the kinetic curve that presented a better fit for the data. Then, these percentages were plotted against their concentrations to determine the required sample concentration to inhibit 50 % collagenase activity (IC_{50}). The data were analysed using Graph Pad Prism Software, and the results were expressed as IC_{50} mean ± SEM.

Anti-elastase activity. The fluorometric Neutrophil Elastase Inhibitor Screening Kit (Abcam; ab118971) was used to evaluate the ability of the extracts, fractions, and subfractions to inhibit the activity of the neutrophil elastase (NE) enzyme. NE was reconstituted with 220 µl of NE assay buffer (AB). SPCK (5, 1, 0.2, 0.04 µM) was used as the positive control. Samples were prepared to have 3 points of concentration in µg/ml for each extract (500, 100, 20), 1 point for each fraction (40), and 4 points for each subfraction (5, 1, 0.2, 0.04). Additionally, the concentration of subfraction 19.1 was tested up to 100 µg/ml. Briefly, 2 µl of reconstituted NE was mixed with 48 µl AB; this mixture (NE-AB) was added to all wells. The reaction wells were prepared according to the manufacturer's instructions: (samples) 50 µl NE-AB + 25 µl sample; (control) 50 µl NE-AB + 25 µl SPCK; (enzyme control) 50 µl NE-AB + 25 µl AB; and (background control) 75 µl AB. The components were mixed in a 96-white opaque plate and incubated for 5 min at 37ºC. Finally, 25 µl of reaction mix (23 µl AB + 2 µl elastase substrate) was added to all wells. RFU were measured at 37ºC with an excitation wavelength of 400 nm and an emission of 505 nm using a microplate reader (FLX800 Biotek) in kinetic mode (60 min). The percentage inhibition of the tested samples was calculated using the slope from the kinetic curve that presented a better fit for the data. Then, in the case of extracts and subfractions, these percentages were plotted against their concentrations to determine the required sample concentration to inhibit 50 % elastase activity (IC_{50}). The data were analysed using Graph Pad Prism Software, and the results were expressed as IC_{50} mean ± SEM (extracts and subfractions) or RFU (fractions).

Anti-tyrosinase activity. The l-Dopa oxidase activity of human tyrosinase was assayed for the extracts and subfractions of *C. hypocistis* following the method described by Mann and colleagues, with some modifications (Mann et al., 2018; WINDER and HARRIS, 1991). The human tyrosinase enzyme (TP321797, Origene) was diluted to 2 µg/ml with the recommended buffer (25 mM Tris–HCl, 100 mM glycine, pH 7.3, 10 % glycerol). Before performing the assay, 5 mM l-Dopa and the assay buffer 0.1 M phosphate, pH 6.8, (AB) were prepared. 4-*n*-Butylresorcinol (8, 4, 1 µM) was used as the positive control (PCT). Serial dilutions (at least $n = 6$) were prepared to have 6 points of concentration in µg/ml for each extract (32, 16, 8, 4, 2, 1) and 5 points for each subfraction (100, 50, 25, 12.5, 6.25). The reaction wells were prepared in 96 optical-bottom plates as follows: (samples) 122 µl AB + 60 µl l-Dopa + 8 µl sample + 10 µl enzyme; (PCT) 122 µl AB + 60 µl l-Dopa + 8 µl PCT + 10 µl enzyme; (enzyme control) 130 µl AB + 60 µl l-Dopa + 10 µl enzyme; and (background control) 140 µl AB + 60 µl l-Dopa. The mixtures were measured (475 nm) at 37ºC using a microplate reader (FLX800 Biotek) in kinetic mode (60 min). The percentage inhibition of the tested samples was calculated using the slope from the kinetic curve that presented a better fit for the data. Then, these percentages were plotted against their concentrations to determine the required sample concentration to inhibit 50 % tyrosinase activity (IC_{50}). The data were analysed using Graph Pad Prism Software, and the results were expressed as IC_{50} mean ± SEM.

Metabolomic profiling studies

LC—HRMS data acquisition and dereplication. The dried extracts and fractions were dissolved in a 20 % ethanol: water solution (20:80, *v/v*) and centrifuged; the resulting supernatants were analysed using LC—HRMS at a final 1 mg/ml concentration, and the solvent was included as a blank. The analysis was conducted as previously described (Macintyre et al., 2014), with slight gradient and running time changes. A binary gradient method (60 min) was utilised: solvent A (water and 0.1 % HCOOH) and B (CH_3CN). The elution was started by the isocratic mode using 15 % B in A (5 min), then changed to the gradient mode using 15–20 % B in A (5 min), 20–25 % B in A (10 min), 25–35 % B (10 min), 35- 50 % B in A (10 min), and then to isocratic mode using 100 % B (10 min). For data split and conversion, the two ionisation modes of the raw files were converted using the MSConvert software and then processed using MZmine 3.2.3.

NMR structural elucidation. The preliminary ^{1}H NMR spectra of extracts and fractions were obtained by a Bruker® AVIII HD 500 (11.7 T) system using CH_3OH-d_4 and $(CH_3)_2SO$-d_6, and D_2O as solvents. The resulting spectral data were then stacked. Chemical shift (δ) values were set between 0.0 and 9.0 ppm and later prepared for output using a bin width of 0.04 ppm and the average sum for bin intensities before multivariate analysis. 2D ^{13}C-^{1}H HSQC and HMBC NMR spectra of bioactive fractions 20 and purified subfractions 19.1 and 19.9 were also measured for further structural elucidation (refer to subfractions preparation in the **SP**). The NMR spectra were processed using MestReNova x64 software (version 14.1.2, Mestrelab Research SL).

Results and discussion

Biochemometric analysis of the crude extracts

Human foreskin fibroblasts (HFF-1) and human immortalised non-tumorigenic keratinocyte (HaCaT) cell lines were selected as model cells to investigate extracts' toxicity towards the skin. The tested extracts exhibited moderate or no toxicity up to the maximum tested concentration (< 400 µg/ml), with the lowest IC_{50} value being 242.4 µg/ml (**Table S2**).

The 3T3-NRU is a validated and regulatory-approved *in vitro* assay to evaluate compounds' photo-safety. Regarding the results, except for extracts C2 (MPE: 0.13) and C3 (MPE: 0.11) from Year 1 (Y1), which were classified as equivocal phototoxic, there is a consensus in the classification as non-phototoxic of the remaining extracts, with PIFs < 2 and MPEs < 0.1 ml (**Table S2**).

The CAA method was applied to measure extracts' antioxidant activity, while their inhibitory potential against three enzymes involved in skin ageing was assessed through direct enzymatic inhibition. The results (IC_{50}) for the antioxidant and enzyme inhibitory properties of the 9 crude extracts are presented in **Table S2**. Fig. 2 illustrates a preliminary analysis of the effect of the foraging year and extraction conditions on these biological activities. The antioxidant responses for both cell lines exhibited comparable values across the nine extracts, indicating that the two conditions did not significantly impact the final response (Fig. 2**A and 2B**). Similarly, the distinct extraction conditions did not significantly influence the enzyme inhibitory properties, as depicted in Fig. 2**D**. Contrarily, the foraging year significantly affected collagenase and elastase activities. As observed in Fig. 2**C**, the Year 2 (Y2) and Year 3 (Y3) collagenase activities were statistically lower than Year 1 (Y1).

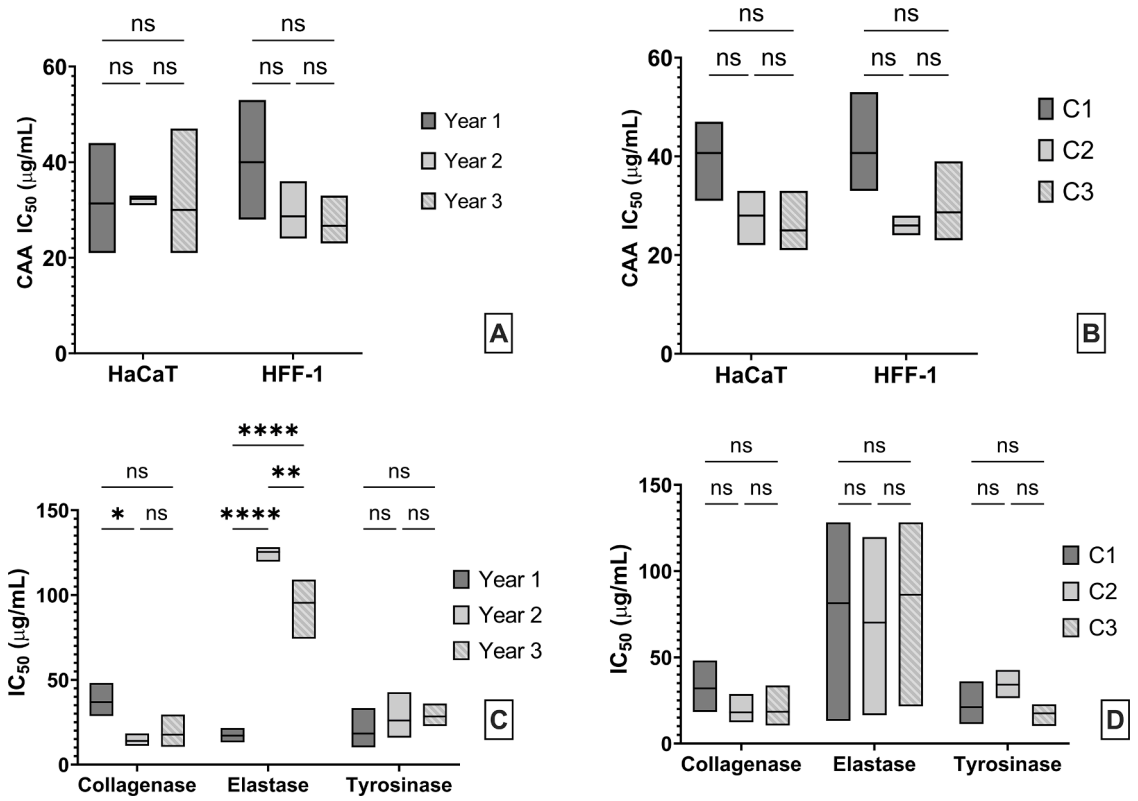

Fig. 2. Boxplot (5–95 percentile; line at mean) of the effects of the foraging year (**A** and **C**) and extraction conditions (**B** and **D**) through a two-way ANOVA followed by a Tukey's multiple comparisons test on the antioxidant and enzyme inhibitory IC_{50s} (µg/ml) of the extracts. Statistical differences (*p-value*): ns (non-significant > *0.05*); *(≤ *0.05*); **(≤ *0.01*); ****(≤ *0.0001*).

Regarding elastase, the IC_{50} also differed among years — particularly Year 1, which presented the lowest IC_{50}, followed by Year 3 and Year 2.

A multivariate analysis was conducted to explore the discriminant features associated with the presence of different metabolites across the three years. The LC—HRMS datasets were subjected to partial least squares discriminant analysis (PLS-DA; Fig. 3**A**), classifying the extracts into three clusters based on their respective foraging years, in alignment with their elastase inhibition (IC_{50} values: Year 1 ranging from 13.2 to 21.6 µg/ml, Year 2 from 74.3 to 109.1 µg/ml, and Year 3 from 119.7 to 128.2 µg/ml). The model obtained showed a high goodness of fit and prediction, with an R^2 of 0.99 and a Q^2 of 0.71. The difference between R^2 and Q^2 was 0.28, indicating no overfitting in the model. The PLS-DA loadings plot (Fig. 3**B**) presents the mass spectral data of the different extracts. Compounds positioned at the intersection of the four quadrants represent the common metabolites among all nine extracts, mainly comprised of medium to high molecular masses. Conversely, compounds aligned with the PLS-DA scores that extend farther from the centre denote the characteristic discriminating features for each year. The most bioactive metabolites (Year 1), encircled in green, displayed an *m/z* range between 500 and 950 Da, indicating medium to high molecular masses. The less active (Year 2), delimited in blue, showed ion peaks for lower molecular weight compounds between 150 and 300 Da. It is possible that the variation in precipitation before the harvest may have caused these differences. As shown in **Table S1**, the average minimum and maximum temperatures were similar in the three years, whereas precipitation was double in Year 1, the year exhibiting the best anti-elastase activity. Interestingly, Year 2 discriminant metabolites (data not shown) were chlorinated organic compounds. The increase in chlorine is part of the plant's adaptive response to use water, nitrogen, and carbon/energy efficiently — significant water-use efficiency improvement results from concurrent growth stimulation and water use reduction. (Colmenero-Flores et al., 2019).

Compounds with the molecular formula $C_{34}H_{24}O_{22}$, $C_{41}H_{28}O_{26}$, and $C_{38}H_{39}Cl_4NO_{18}$ were ascribed as the most discriminant features for Year 1 (*p*-values < 0.05). The first and second compounds were identified as ellagitannins, with $[M-H]^-$ ion peaks at *m/z* 783.068 and 935.079 Da, respectively. Although no compound hits identified were related to the Cytinaceae family, previous publications pointed to hydrolysable tannins, such as ellagitannins, as the metabolites behind *C. hypocistis* bioactive properties (Silva et al., 2022, 2020). Year 1 dereplicated discriminating features and their structures are provided in **Table S3** and **Figure S2**, respectively.

Biochemometric analysis of the fractions

Based on the biochemometric integration of the crude extracts and to validate the putative discriminating features identified in Year 1, a bioassay-guided fractionation approach of the hydroethanolic extracts exhibiting the best (C1, C2, and C3 – Year 1) and worst anti-elastase activities (C3 – Year 2) was performed. All fractions were analysed through LC—HRMS and evaluated for their anti-elastase activity, followed by multivariate analysis to integrate the data. Fractions exhibiting the highest elastase inhibition were also tested for their antioxidant properties. Fig. 4**A** illustrates the anti-elastase activity; all fractions displayed a strong ability to inhibit elastase at 40 µg/ml, evident from the decrease in the RFU compared to the bar exhibiting 100 % activity. Fractions 5, 6, 7, 18, 19, 20, 30, and 31 presented the highest inhibitions, with percentages superior to 96 % (**Table S4**). These eight fractions are associated with Year 1 fractions eluted within the 40 % to 60 % ethanol range. Fig. 4**B** presents the statistical differences among the most potent anti-elastase activities. Fractions 6, 19, 20, and 30 exhibited the best inhibitory results among all tested samples.

Considering the pivotal role of ROS in activating skin ageing pathways (Papaccio et al., 2022), the assessment of ROS inhibition in HaCaT

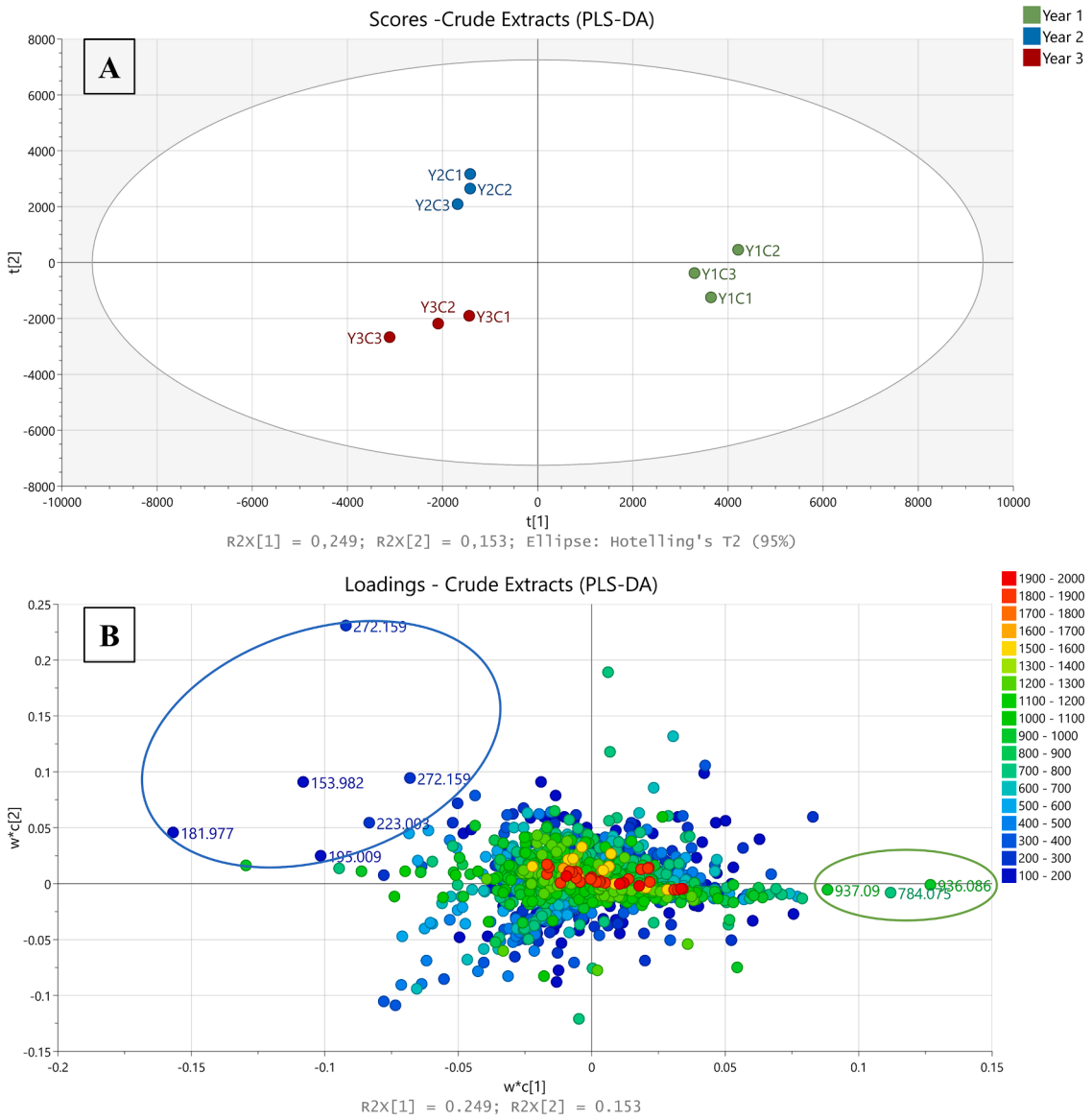

Fig. 3. (A) PLS-DA scores of the extracts classified according to their foraging year and (B) loadings plot of the LC—HRMS data. The R^2 and Q^2 values were 0.99 and 0.71, respectively. Encircled features in green and blue indicate the discriminating features of the most (Y1) and least (Y2) active extracts against elastase, respectively.

cells was also included in the bioactive properties tested for fractions exhibiting the best elastase inhibition. This strategy aimed to prioritise the selection of fractions with multifunctional properties for subsequent purification. Fig. 5 illustrates the differences in the IC_{50s} among the eight fractions tested (> 96 % inhibition). Fraction 20 exhibited the lowest IC_{50} (μg/ml), 5.74 ± 0.29, followed by fractions 18 (8.09 ± 0.56) and 19 (10.39 ± 0.41).

The anti-elastase and antioxidant results revealed a consistent tendency, where fractions 19 and 20 emerged among the samples displaying the best bioactivity. The LC—HRMS data were subjected to supervised orthogonal partial least squares discriminant analysis (OPLS-DA) to identify compounds correlated with the anti-elastase results. The fractions were categorised into two classes: high anti-elastase activity (Y1: 5, 6, 7, 18, 19, 20, 30, and 31) and low anti-elastase activity (remaining fractions). Fig. 6**A** illustrates the OPLS-DA score plot, which separates the fractions into two clusters. The eight most bioactive fractions against elastase were predominantly positioned along the intersection of the left quadrants. Fraction 20 displayed a slight deviation from the other fractions, possibly linked to a subtle variance in its chemical profile. This difference could account for its demonstrated significant antioxidant and anti-elastase activities. Aligned with these observations, the inter-group variation (R2X [1]) accounted for 10 %, while the intra-group variation (R2Xo [1]) was 23 %. These metrics highlight a moderate diversity within groups and are less pronounced than expected between groups. The diversity within groups could be attributed to the significant variability in the chemical profiles within the low anti-elastase activity group (highlighted in blue). This group encompasses Year 1 fractions with the lowest activity and fractions from Year 2, which differ chemically from Year 1, as illustrated by the PLS-DA in Fig. 3. Despite the variation in intra and inter-groups not being optimal, the model obtained showed a high goodness of fit and prediction, with an R^2 of 0.79 and a Q^2 of 0.66. The difference between R^2 and Q^2 was 0.13, indicating no overfitting in the model.

The S-plot (Fig. 6**B**) shows the mass spectral data of the fractions tested for the anti-elastase activity. The metabolites encircled in green correspond to the compounds associated with the fractions exhibiting the best inhibition. Similar to the crude extracts, the eight discriminating metabolites (with the lowest *p*-values) were ascribed as

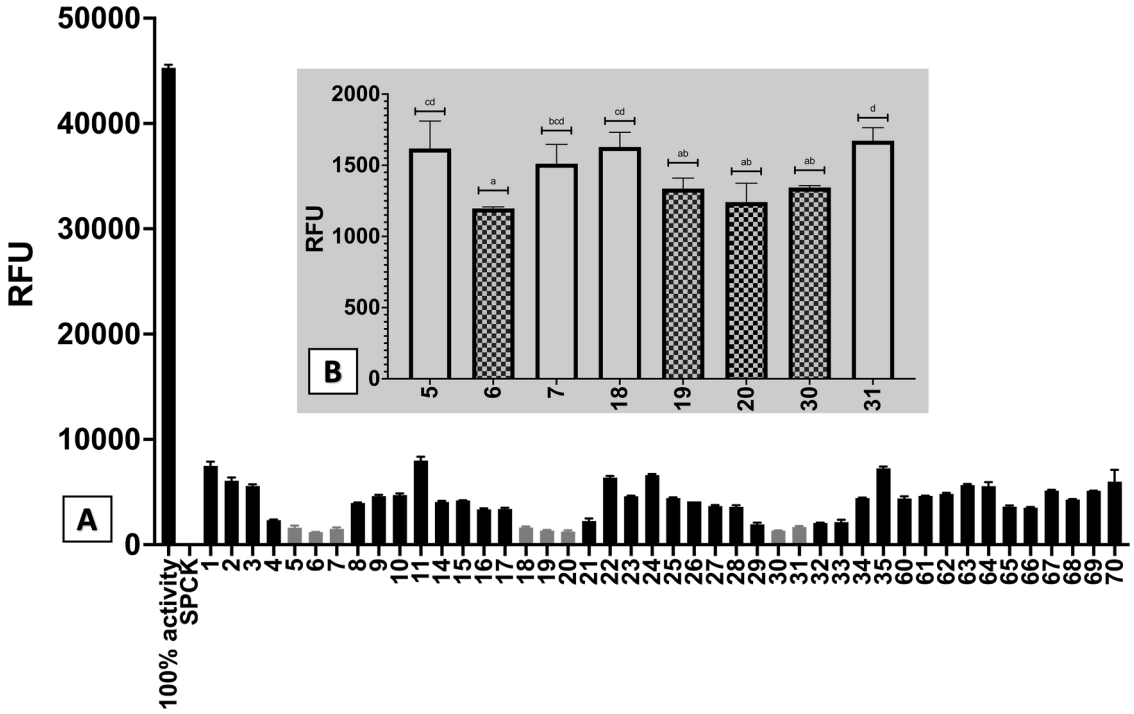

Fig. 4. Graphical representation of the elastase activity (RFU), comprising (**A**) Fractions from Y1 (1–35), Year 2 (60–70), negative control (100 % activity), and positive control (SPCK). (**B**) One-way ANOVA analysis followed by a Tukey's multiple comparisons test for fractions displaying inhibition percentages superior to 96 % (5, 6, 7, 18, 19, 20, 30, and 31). Different letters correspond to significant differences ($p < 0.05$) among samples.

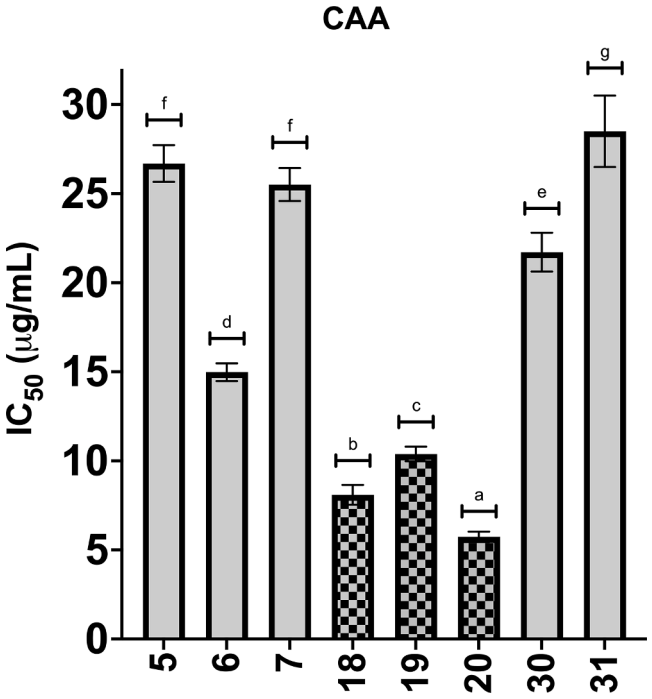

Fig. 5. Graphical representation of the one-way ANOVA analysis followed by a Tukey's multiple comparisons test for the antioxidant activity (IC_{50s}) of fractions displaying the highest anti-elastase activity (5, 6, 7, 18, 19, 20, 30, and 31). Different letters correspond to significant differences ($p < 0.05$) among samples.

ellagitannins (Table 1).

After dereplication, four MZmine IDs were confirmed to have the molecular formula $C_{34}H_{24}O_{22}$ (twelve hits), while the other four were assigned the formula $C_{27}H_{20}O_{18}$ (three hits). Among the twelve compound hits from the first molecular formula, terflavin B had been previously documented in *C. hypocistis* by Zengin and colleagues, who performed an extensive chemical analysis utilising UPLC-ESI-QTOF-MS (Zengin et al., 2022). Pedunculagin was also tentatively identified in a previous publication through HPLC-DAD-ESI/MS^n (Silva et al., 2020).

Regarding the molecular formula $C_{27}H_{20}O_{18}$, terflavin D emerges as a candidate among the three putative compound hits since terflavins are biogenetically related tannins and commonly co-occur within the same species (Lin et al., 1990).

Purification and bioactive validation

As previously stated, fractions 19 and 20 exhibited the most interesting results across the tested biological activities and demonstrated analogous distinguishing characteristics in the multivariate analysis. Furthermore, both fractions displayed similar peak intensities and ^1H NMR spectral data (data not shown) for the discriminant metabolites, positively influencing the anti-elastase activity. Consequently, F19 (from $Y1C_2$) was selected for subsequent purification, primarily due to its higher yield (186 mg) compared to F20 (13 mg). Ten subfractions were obtained, but only P19.1 and P19.9 presented the necessary mass for NMR elucidation and to be assessed for their biological activities (Table 2).

Except for the collagenase positive control, P19.9 presented better antioxidant and enzyme inhibitory properties than P19.1, the crude extract, and the positive controls. Remarkably, P19.9 exhibited a tenfold improvement in elastase inhibition efficacy compared to Y_1C_2; its effectiveness fell within the same range as SPCK, a potent irreversible elastase inhibitor.

Regarding the safety of the purified subfractions, subfraction 19.1 displayed no cytotoxicity and no phototoxicity at concentrations up to 200 and 400 µg/ml, respectively. Conversely, P19.9 presented cytotoxicity solely against HaCaT cells, with an IC_{50} of 133.9 µg/ml, significantly inferior to all bioactive IC_{50s}. No phototoxicity was observed for P19.9.

Fig. 7**A** shows the 2D NMR spectral dataset, which confirmed that the

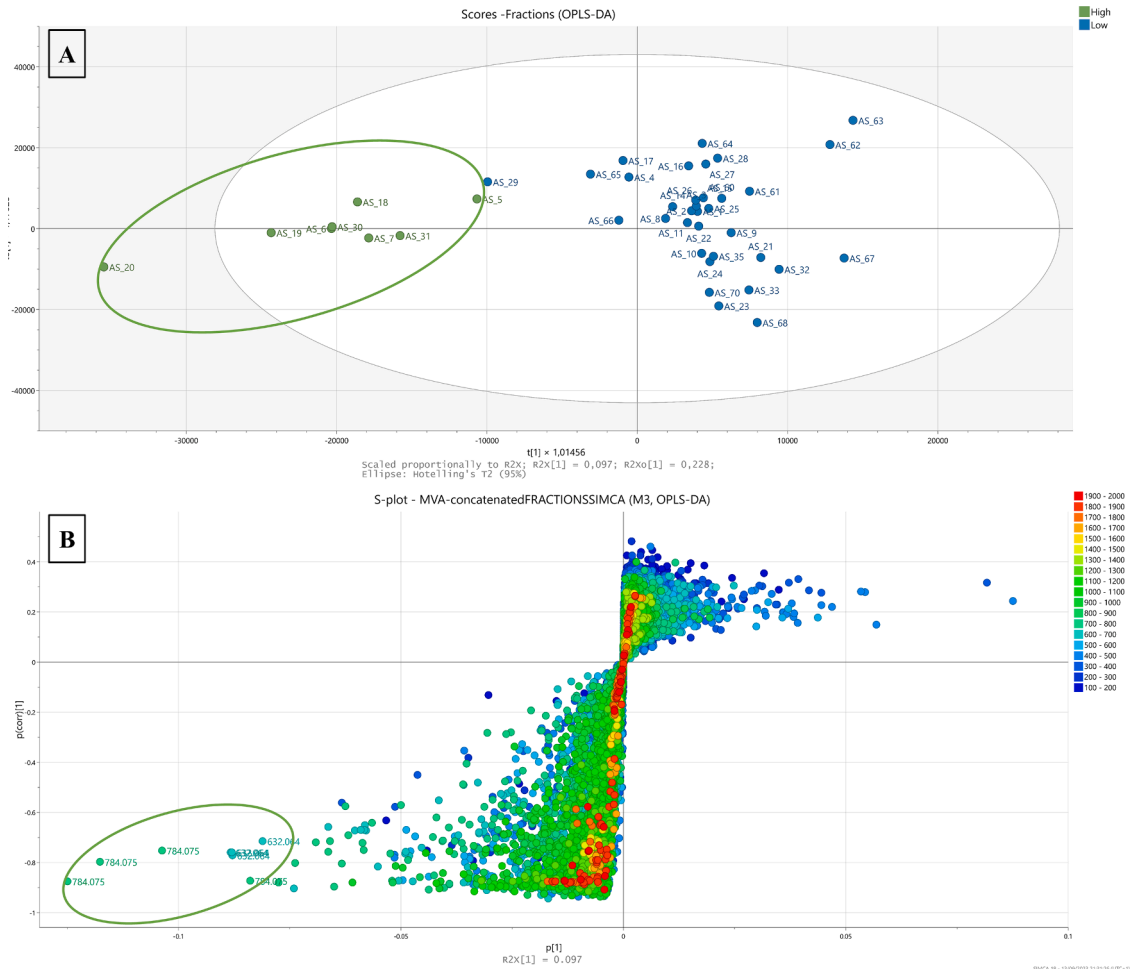

Fig. 6. (**A**) OPLS-DA scores and (**B**) S-plot spectral data of the fractions tested for their anti-elastase activity. The R^2 and Q^2 values were 0.79 and 0.66, respectively. Encircled features in green and blue indicate the discriminating features of the most (High) and least (Low) active fractions against elastase, respectively.

compound present in P19.1 is a galloyl glucose derivative with a molecular formula of $C_{34}H_{24}O_{22}$, and annotated as 2,3:4,6-bis(hexahydroxydiphenoyl)glucose. P19.9 was identified as a galloyl glucose congener based on spectral resonances of pedunculagin rather than terflavin B as predicted (Feldman and Sahasrabudhe, 1999). The lone methine proton at C-2 on the trihydroxy phenolic galloyl ring (δ_H 6.8 and δ_C 110.0) was correlated with the carboxylic ketone group at 166.2 ppm, 109.6 ppm for C-6, and 138.9 ppm for C-4. However, according to the LC—HRMS data from the pre-purified fraction and the broad peaks from ^{1}H NMR (Fig. 7), the subfraction P19.9 seems to be a mixture of *α*- and *β*-pedunculagin with degradation products, as the NMR data indicated. These compounds are inseparable due to the lack of *O*-1 substituents, existing in equilibrium as *α*- and *β*-hemiacetal glycopyranoses. The signals δ_H 6.0 and δ_C 92.3 (Tsujita et al., 2017) could indicate the presence of olefinic protons typically found in oxidation products of aromatic rings. Additionally, olefinic protons interfere with the ^{1}H NMR signals at 5.5 and 5.2, corresponding to the protons of both epimers at C1, which are not well-defined.

The strong intensities of the HMBC cross peaks ($\delta_H \rightarrow \delta_C$) indicated a major compound with a *S,S* configuration as found in the pedunculagin. The axial chiral HHDP (hexahydroxydiphenoyl)-units of the 2,3- and 4,6-*O*-HHDP ellagitannins typically exhibit the (S_a)-configuration, with only two exceptions (cuspinin and platycaryanin) among more than 500 structurally characterised compounds (Immel and Khanbabaee, 2000). Additionally, potentillin and casuarictin, which present (S_a, S_a)-*α*-d-glucopyranose and (S_a,S_a)-*β*-d-glucopyranose, respectively, are recognised precursors of *α*- and *β*- pedunculagin (Okuda et al., 1984, 1983; Tamura et al., 2010).

Pedunculagin has already been described as a neutrophil elastase inhibitor (IC_{50} of 2.8 μM). The docking results provided by the authors suggested that pedunculagin is too large to fit into the elastase biding site and cannot form specific interactions with binding site residues; therefore, inhibition may have occurred due to the coverage of the hydrophobic S1 pocket and active site (Hrenn et al., 2006). The present work obtained an IC_{50} of 0.1 μg/ml, which for a compound with a molecular weight of 784,075 Da, corresponds to 0.13 μM. The IC_{50} differences could be associated with the methodology (colourimetric vs fluorimetric) or the compound (purity and/or structural configuration). Ellagitannins, such as pedunculagin, present an ideal framework as inhibitors of human neutrophil elastase. This is attributed to their glucosyl core linked to HHDP moieties, which play a crucial role in establishing π-π interactions with the aromatic side chains of the enzyme (Ebrahim et al., 2022).

Hydrolysable tannins, including pedunculagin, are known for their multiple biological activities, such as antitumor, antioxidant, gastroprotective, hepatoprotective, and anti-inflammatory properties (Al-Sayed and Esmat, 2016). Studies have shown that pedunculagin can induce the release of TNF-α by inflammatory cells, a cytokine known to act on endothelial cells to induce VEGF production and enhance endothelial cell proliferation and migration, leading to angiogenesis and wound healing (Fernandes et al., 2024). Pedunculagin has also been reported to have photo-chemo-preventive and anti-inflammatory effects in keratinocytes by inhibiting UVB-induced modulations of the NF-kB, STAT/JAK, and MAPK pathways (Yin et al., 2019).

Table 1
Dereplication of the discriminating metabolites from the fractions exhibiting the best (*High group*) anti-elastase activity.

MZmine ID	*m/z*	Rt	MW	Molecular formula	Dereplicated identity	*p*-value	Average (High)	Average (Low)	Fold change
P7124	785,082	6,71	784,075	$C_{34}H_{24}O_{22}$	2,3:4,6-Bis(hexahydroxydiphenoyl)glucose **(1)** 2,3:4,6-Bis(hexahydroxydiphenoyl)glucose; (S_a,S_a)-form (Pedunculagin) 2,3:4,6-Bis(hexahydroxydiphenoyl)glucose; (2,3-R_a:4,6-S_a)-β-d-pyranose-form 2,3:4,6-Bis(hexahydroxydiphenoyl)glucose; (S_a,S_a)-β-d-pyranose-form 2,3:4,6-Bis(hexahydroxydiphenoyl)glucose; (S_a,S_a)-α-d-pyranose-form Casuarinin; 5-degalloyl **(2)** Casuarinin; 1-epimer, 5-*O*-degalloyl 2-*O*-Galloyl 3-*O*-valoneoyldilactoneglucose **(3)** Isooenothein C Oenothein C **(4)** Platycaryanin D **(5)** Terflavin D; 6′-*O*-(3,4,5-trihydroxybenzoyl) (Terflavin B) **(6)**	$1{,}78E^{-12}$	6,176,410	1,087,360	5,68
P9430	785,083	11,07	784,075	Same as P7124		$3{,}33E^{-12}$	2,743,330	460,382	5,96
P7236	785,082	6,81	784,075	Same as P7124		$3{,}90E^{-09}$	6,196,540	1,305,650	4,75
P4556	633,071	3,03	632,064	$C_{27}H_{20}O_{18}$	Castalin **(14)** Cauliflorin **(15)** Terflavin D **(16)**	$5{,}52E^{-09}$	3,730,100	831,378	4,49
P6895	785,082	6,52	784,075	Same as P7124		$1{,}75E^{-08}$	4,714,650	586,804	8,03
P4731	633,071	3,03	632,064	Same as P4556		$3{,}72E^{-08}$	3,749,510	874,280	4,29
P4913	633,071	3,05	632,064	Same as P4556		$4{,}60E^{-08}$	3,774,960	885,077	4,27
P5116	633,071	3,08	632,064	Same as P4556		$7{,}42E^{-07}$	3,485,490	917,925	3,80

MZmine ID: The letter P represents the positive ionisation mode, whereas the number is the metabolite MZmine identification; ***m/z***: Ratio mass to charge; **Rt**: Retention time; **Dereplicated Identity**: Compound hits can be interchangeable for identical molecular formulae; ***p*-value**: Statistical significance of a specific compound's role in the anti-elastase activity; **Average (High/Low)**: Peak intensities average in each group; **Fold change**: Peak intensities differences between groups; **(number)**: compound structures are provided in the SP.

Table 2
Cytotoxic, phototoxic, antioxidant, and enzyme inhibitory properties of *C. hypocistis* P19.1 and P19.9, compared with their origin crude extract (Y_1C_2) and controls.

	Y_1C_2	P19.1	P19.9	Controls
	Cytotoxic activity (IC_{50}, µg/ml)			
HaCaT	250.1 ± 4.9	>200	133.9 ± 3.8	–
HFF-1	>400	>200	>200	–
	3T3 Neutral Red Uptake (NRU) phototoxicity activity			**CPZ**
PIF	1.5 (NP)	NP	1.763 (NP)	8.14
MPE	0.13 (EP)		−0.042 (NP)	0.172
	Cellular antioxidant activity (IC_{50}, µg/ml)			**AA**
HaCaT	29.0 ± 2.8[b]	67.9 ± 2.4[c]	5.3 ± 0.4[a]	231.20 ± 0.04[d]
HFF-1	28.2 ± 4.9[b]	97.1 ± 3.6[c]	4.3 ± 0.2[a]	115.00 ± 0.02[d]
	Anti-collagenase activity (IC_{50}, µg/ml)			**Phe**
Bacterial collagenase	28.7 ± 2.9[c]	33.7 ± 4.2[c]	18.4 ± 2.6[b]	8.5 ± 0.3[a]
	Anti-elastase activity (IC_{50}, µg/ml)			**SPCK**
Human elastase	16.5 ± 1.0[b]	>100	0.10 ± 0.02[a]	0.07 ± 0.01[a]
	Anti-tyrosinase activity (IC_{50}, µg/ml)			**Butyl**
Human tyrosinase	33.3 ± 0.1[c]	71.4 ± 1.0[d]	9.3 ± 0.6[b]	1.0 ± 0.1[a]

PIF: photo irritation factor; **MPE**: mean photo effect; **Non-phototoxicity – NP** (PIF < 2 or MPE < 0.1); **Equivocal phototoxicity – EP** (2 < PIF < 5 or 0.1 < MPE < 0.15); **Phototoxicity** (PIF > 5 or MPE > 0.15); **CPZ**: chlorpromazine; **AA:** ascorbic acid; **Phe**: 1,10-phenanthroline; **SPCK**: MeOSuc-Ala-Ala-Pro-Val-chloromethylketone; **Butyl**: 4-*n*-butylresorcinol; Different letters correspond to significant differences ($p < 0.05$) among samples from ANOVA analysis followed by Tukey's multiple comparisons test.

Conclusions

This study established that the chemical composition of *C. hypocistis* and its anti-ageing properties were significantly affected by the harvest year. Using a biochemometric approach, it was observed that the variation in neutrophil elastase inhibition between years was due to compound 2,3:4,6-bis(hexahydroxydiphenoyl)glucose, with a molecular weight of 784.075 Da. Upon structural elucidation, it became apparent that the subfraction contained a blend of α- and β-pedunculagin epimers of pedunculagin. Moreover, this subfraction displayed no cytotoxicity or phototoxicity and excellent efficacy for the tested anti-ageing properties. Remarkably, a tenfold improvement in neutrophil elastase inhibition efficacy was observed compared to the crude extract, with a similar result to SPCK, a potent irreversible neutrophil elastase inhibitor.

Funding

The authors are grateful to the Foundation for Science and Technology (FCT, Portugal) for financial support through national funds FCT/MCTES (PIDDAC) to CIMO (UIDB/00690/2020 and UIDP/00690/2020) and SusTEC (LA/P/0007/2020). A. R. Silva is grateful to FCT and FSE for her Doctoral Grant (SFRH/BD/145,834/2019), and L. Barros for her institutional scientific employment program-contract.

CRediT authorship contribution statement

Ana Rita Silva: Writing – original draft, Methodology, Investigation, Formal analysis, Data curation, Conceptualization. **Manuel Ayuso:** Writing – review & editing, Methodology, Formal analysis. **Pablo A. García:** Writing – review & editing. **Lillian Barros:** Writing – review & editing, Funding acquisition, Conceptualization. **RuAngelie Edrada-Ebel:** Writing – review & editing, Methodology, Conceptualization.

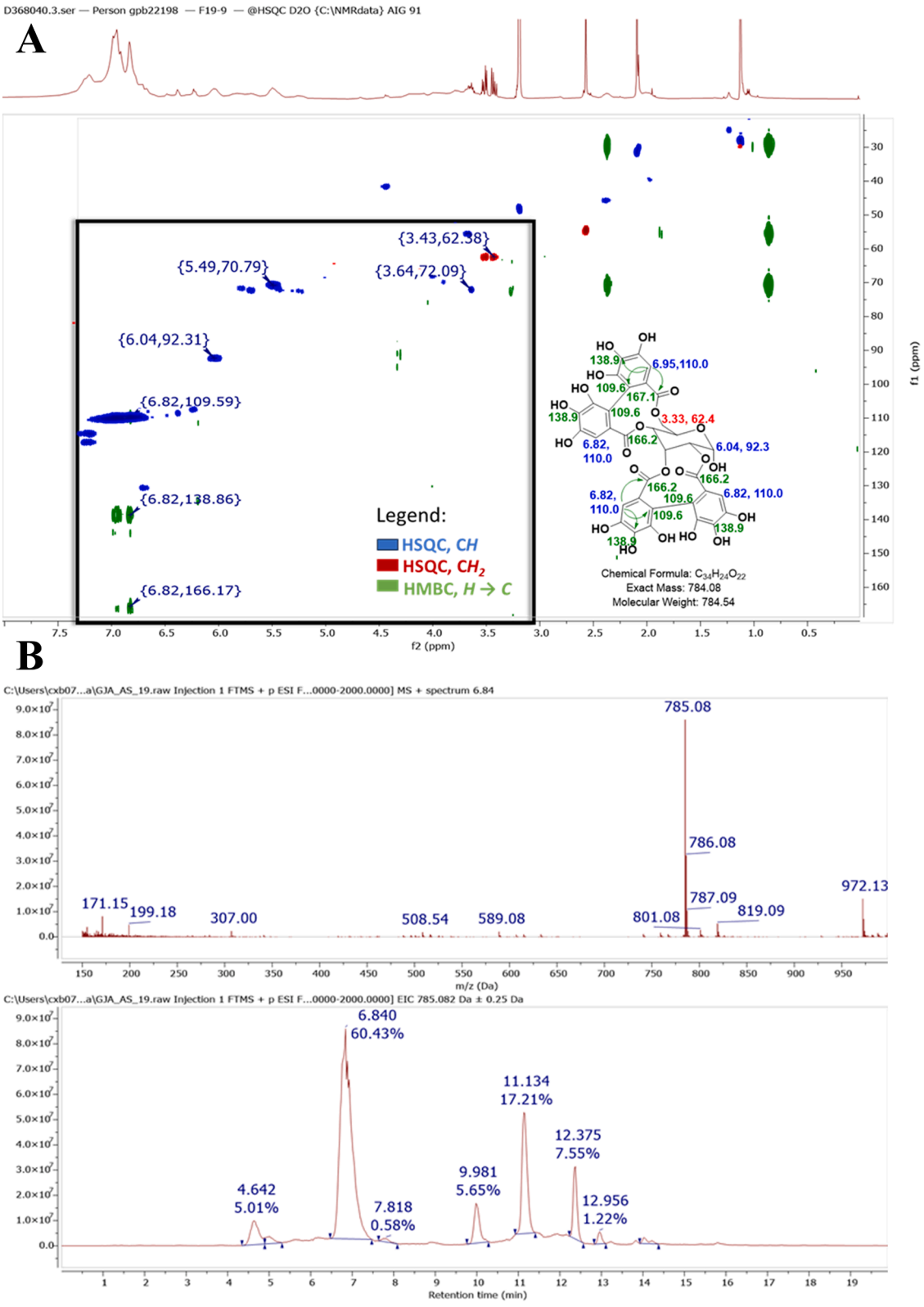

Fig. 7. (**A**) Superimposed 2D HSQC and HMBC NMR data (in D_2O, 500 MHz) of semi-purified biologically active galloyl glucose congener found in P19.9. (**B**) High-resolution mass spectral data from the peak at 6.84 min of F19 (above) corresponding to a mixture of galloyl glucose congeners in *C. hypocistis* and chromatogram of F19 before purification (below).

Declaration of competing interest

The authors declare that they have no known competing financial interests or personal relationships that could have appeared to influence the work reported in this paper.

Supplementary materials

Supplementary material associated with this article can be found, in the online version, at doi:10.1016/j.phymed.2024.155685.

References

Al-Sayed, E., Esmat, A., 2016. Hepatoprotective and antioxidant effect of ellagitannins and galloyl esters isolated from Melaleuca styphelioides on carbon tetrachloride-induced hepatotoxicity in HepG2 cells. Pharm. Biol. 54, 1727–1735. https://doi.org/10.3109/13880209.2015.1125933.

Caesar, L.K., Cech, N.B., 2019. Synergy and antagonism in natural product extracts: when 1 + 1 does not equal 2. Nat. Prod. Rep. 36, 869. https://doi.org/10.1039/C9NP00011A.

Colmenero-Flores, J.M., Franco-Navarro, J.D., Cubero-Font, P., Peinado-Torrubia, P., Rosales, M.A., 2019. Chloride as a beneficial macronutrient in higher plants: new roles and regulation. Int. J. Mol. Sci. 20 https://doi.org/10.3390/IJMS20194686.

Działo, M., Mierziak, J., Korzun, U., Preisner, M., Szopa, J., Kulma, A., 2016. The potential of plant phenolics in prevention and therapy of skin disorders. Int. J. Mol. Sci. 17 https://doi.org/10.3390/IJMS17020160.

Ebrahim, H.Y., Mady, M.S., Atya, H.B., Ali, S.A., Elsayed, H.E., Moharram, F.A., 2022. Melaleuca rugulosa (Link) Craven Tannins: appraisal of anti-inflammatory, radical scavenging activities, and molecular modeling studies. J. Ethnopharmacol. 298, 115596 https://doi.org/10.1016/J.JEP.2022.115596.

Enke, C.G., Nagels, L.J., 2011. Undetected components in natural mixtures: how many? What concentrations? Do they account for chemical noise? What is needed to detect them? Anal. Chem. 83, 2539–2546. https://doi.org/10.1021/AC102818A/SUPPL_FILE/AC102818A_SI_001.PDF.

Feldman, K.S., Sahasrabudhe, K., 1999. Ellagitannin chemistry. Syntheses of Tellimagrandin II and a Dehydrodigalloyl Ether-containing Dimeric Gallotannin analogue of Coriariin A. J. Org. Chem. 64, 209–216. https://doi.org/10.1021/jo9816966.

Fernandes, A.S., de Melo Bisneto, A.V., Silva, L.S., Bailão, E.F.L.C., Cardoso, C.G., Carneiro, C.C., da Costa Santos, S., Chen-Chen, L., 2024. Pedunculagin and tellimagrandin-I stimulate inflammation and angiogenesis and upregulate vascular endothelial growth factor and tumor necrosis factor-alpha in vivo. Microvasc. Res. 151, 104615 https://doi.org/10.1016/J.MVR.2023.104615.

Flament, F., Bazin, R., Laquieze, S., Rubert, V., Simonpietri, E., Piot, B., 2013. Effect of the sun on visible clinical signs of aging in Caucasian skin. Clin. Cosmet. Invest. Dermatol. 6, 221–232. https://doi.org/10.2147/CCID.S44686.

Guimarães, R., Barros, L., Dueñas, M., Calhelha, R.C., Carvalho, A.M., Santos-Buelga, C., Queiroz, M.J.R.P., Ferreira, I.C.F.R., 2013. Nutrients, phytochemicals and bioactivity of wild Roman chamomile: a comparison between the herb and its preparations. Food Chem. 136, 718–725. https://doi.org/10.1016/j.foodchem.2012.08.025.

Hrenn, A., Steinbrecher, T., Labahn, A., Schwager, J., Schempp, C.M., Merfort, I., 2006. Plant phenolics inhibit neutrophil elastase. Planta Med. 72, 1127–1131. https://doi.org/10.1055/S-2006-946700/ID/2/BIB.

Immel, S., Khanbabaee, K., 2000. Atropdiastereoisomers of ellagitannin model compounds: configuration, conformation, and relative stability of D-glucose diphenoyl derivatives. Tetrahedron Asymmetry 11, 2495–2507. https://doi.org/10.1016/S0957-4166(00)00179-8.

Kellogg, J.J., Todd, D.A., Egan, J.M., Raja, H.A., Oberlies, N.H., Kvalheim, O.M., Cech, N. B., 2016. Biochemometrics for Natural Products Research: comparison of Data Analysis Approaches and Application to Identification of Bioactive Compounds. J. Nat. Prod. 79, 376–386. https://doi.org/10.1021/ACS.JNATPROD.5B01014/SUPPL_FILE/NP5B01014_SI_001.PDF.

Lerman, I., Hammes, S.R., 2018. Neutrophil elastase in the tumor microenvironment. Steroids 133, 96–101. https://doi.org/10.1016/J.STEROIDS.2017.11.006.

Liao, W., Ning, Z., Chen, L., Wei, Q., Yuan, E., Yang, J., Ren, J., 2014. Intracellular antioxidant detoxifying effects of diosmetin on 2,2-azobis(2-amidinopropane) dihydrochloride (AAPH)-induced oxidative stress through inhibition of reactive oxygen species generation. J. Agric. Food Chem. 62, 8648–8654. https://doi.org/10.1021/JF502359X/ASSET/IMAGES/MEDIUM/JF-2014-02359X_0002.GIF.

Lin, T.chen, Nonaka, G.ichiro, Nishioka, I., Ho, F.chi, 1990. Tannins and related compounds. CII. : structures of Terchebulin, an Ellagitannin having a novel Tetraphenylcarboxylic Acid(Terchebulic Acid)Moiety, and biogenetically related tannins from Terminalia chebula RETZ. Chem. Pharm. Bull. (Tokyo) 38, 3004–3008. https://doi.org/10.1248/CPB.38.3004.

MacDonald-Wicks, L.K., Wood, L.G., Garg, M.L., 2006. Methodology for the determination of biological antioxidant capacity in vitro: a review. J. Sci. Food Agric. 86, 2046–2056. https://doi.org/10.1002/jsfa.2603.

Macintyre, L., Zhang, T., Viegelmann, C., Martinez, I.J., Cheng, C., Dowdells, C., Abdelmohsen, U.R., Gernert, C., Hentschel, U., Edrada-Ebel, R.A., 2014. Metabolomic tools for secondary metabolite discovery from marine microbial symbionts. Mar. Drugs 2014 12, 3416–3448. https://doi.org/10.3390/MD12063416, 12, 3416–3448.

Mani, J., Johnson, J., Hosking, H., Hoyos, B.E., Walsh, K.B., Neilsen, P., Naiker, M., 2022. Bioassay guided fractionation protocol for determining novel active compounds in selected australian flora. Plants 11. https://doi.org/10.3390/PLANTS11212886.

Mann, T., Scherner, C., Röhm, K.H., Kolbe, L., 2018. Structure-activity relationships of thiazolyl resorcinols, potent and selective inhibitors of human Tyrosinase. Int. J. Mol. Sci. 19 https://doi.org/10.3390/IJMS19030690.

Najmi, A., Javed, S.A., Al Bratty, M., Alhazmi, H.A, 2022. Modern approaches in the discovery and development of plant-based natural products and their analogues as potential therapeutic agents. Molecules 27. https://doi.org/10.3390/MOLECULES27020349.

Nunes, A., Marto, J., Gonçalves, L.M., Simões, S., Félix, R., Ascenso, A., Lopes, F., Ribeiro, H.M., 2020. Novel and modified neutrophil elastase inhibitor loaded in topical formulations for psoriasis management. Pharmaceutics 12. https://doi.org/10.3390/PHARMACEUTICS12040358.

Okuda, T., Yoshida, T., Ashida, M., Yazaki, K., 1983. Tannis of Casuarina and Stachyurus species. Part 1. Structures of pendunculagin, casuarictin, strictinin, casuarinin, casuariin, and stachyurin. J. Chem. Soc. Perkin 1 (0), 1765–1772. https://doi.org/10.1039/P19830001765.

Okuda, T., Yoshida, T., Kuwahara, M., Memon, U., Shingu, T., 1984. Tannins of Rosaceous Medicinal Plants. I. Structures of Potentillin, Agrimonic Acids A and B, and Agrimoniin, a Dimeric Ellagitannin. Chem. Pharm. Bull. (Tokyo) 32, 2165–2173. https://doi.org/10.1248/CPB.32.2165.

Papaccio, F., D'arino, A., Caputo, S., Bellei, B., 2022. Focus on the contribution of oxidative stress in skin aging. Antioxidants 11. https://doi.org/10.3390/ANTIOX11061121.

Pittayapruek, P., Meephansan, J., Prapapan, O., Komine, M., Ohtsuki, M., 2016. Role of matrix metalloproteinases in photoaging and photocarcinogenesis. Int. J. Mol. Sci. 17 https://doi.org/10.3390/IJMS17060868.

Rahman, S., Ul Haq, F., Ali, A., Khan, M.N., Shah, S.M.Z., Adhikhari, A., El-Seedi, H.R., Musharraf, S.G, 2019. Combining untargeted and targeted metabolomics approaches for the standardization of polyherbal formulations through UPLC–MS/MS. Metabolomics 15, 1–11. https://doi.org/10.1007/S11306-019-1582-6/TABLES/3.

Russell-Goldman, E., Murphy, G.F., 2020. The pathobiology of skin aging: new insights into an old dilemma. Am. J. Pathol. 190, 1356–1369. https://doi.org/10.1016/J.AJPATH.2020.03.007.

Sanjust, E., Rinaldi, A.C., 2021. Cytinus under the microscope: disclosing the secrets of a parasitic plant. Plants 10, 146. https://doi.org/10.3390/plants10010146.

Silva, A.R., Ayuso, M., Pereira, C., Dias, M.I., Kostić, M., Calhelha, R.C., Soković, M., García, P.A., Ferreira, I.C.F.R., Barros, L., 2022. Evaluation of parasite and host phenolic composition and bioactivities – the practical case of *Cytinus hypocistis* (L.) L. and *Halimium lasianthum* (Lam.) greuter. Ind. Crops Prod. 176, 114343 https://doi.org/10.1016/J.INDCROP.2021.114343.

Silva, A.R., Fernandes, Â., García, P.A., Barros, L., Ferreira, I.C.F.R., 2019. *Cytinus hypocistis* (L.) L. subsp. *macranthus* Wettst.: nutritional characterization. Molecules 24, 1111. https://doi.org/10.3390/molecules24061111.

Silva, A.R., Pinela, J., Dias, M.I., Calhelha, R.C., Alves, M.J., Mocan, A., García, P.A., Barros, L., Ferreira, I.C.F.R., 2020. Exploring the phytochemical profile of *Cytinus hypocistis* (L.) L. as a source of health-promoting biomolecules behind its in vitro bioactive and enzyme inhibitory properties. Food Chem. Toxicol. 136, 111071 https://doi.org/10.1016/j.fct.2019.111071.

Silva, A.R., Pinela, J., García, P.A., Ferreira, I.C.F.R., Barros, L., 2021. *Cytinus hypocistis* (L.) L.: optimised heat/ultrasound-assisted extraction of tannins by response surface methodology. Sep. Purif. Technol. 276, 119358 https://doi.org/10.1016/j.seppur.2021.119358.

Tamura, S., Yang, G.M., Yasueda, N., Matsuura, Y., Komoda, Y., Murakami, N., 2010. Tellimagrandin I, HCV invasion inhibitor from Rosae Rugosae Flos. Bioorg. Med. Chem. Lett. 20, 1598–1600. https://doi.org/10.1016/J.BMCL.2010.01.084.

Test No. 432, 2019. Vitro 3T3 NRU Phototoxicity Test. OECD Guidelines for the Testing of Chemicals, Section 4. OECD. https://doi.org/10.1787/9789264071162-EN.

Tsujita, T., Matsuo, Y., Saito, Y., Tanaka, T., 2017. Enzymatic oxidation of ellagitannin and a new ellagitannin metabolite from Camellia japonica leaves. TetrahedronTetrahedron 73, 500–507. https://doi.org/10.1016/J.TET.2016.12.027.

Veiga, M., Costa, E.M., Silva, S., Pintado, M., 2020. Impact of plant extracts upon human health: a review. Crit. Rev. Food Sci. Nutr. 60, 873–886. https://doi.org/10.1080/10408398.2018.1540969.

Voynow, J.A., Shinbashi, M., 2021. Neutrophil Elastase and chronic lung disease. Biomolecules 11. https://doi.org/10.3390/BIOM11081065.

WINDER, A.J., HARRIS, H., 1991. New assays for the tyrosine hydroxylase and dopa oxidase activities of tyrosinase. Eur. J. Biochem. 198, 317–326. https://doi.org/10.1111/J.1432-1033.1991.TB16018.X.

Yin, J., Kim, H.H., Hwang, I.H., Kim, D.H., Lee, M.W., 2019. Anti-inflammatory effects of phenolic compounds isolated from Quercus Mongolica Fisch. ex Ledeb. on UVB-irradiated human skin cells. Molecules 2019, Vol. 24, Page 3094. https://doi.org/10.3390/MOLECULES24173094, 24, 3094.

Zengin, G., Cádiz-Gurrea, M., de la, L., Fernández-Ochoa, Á., Leyva-Jiménez, F.J., Carretero, A.S., Momotko, M., Yildiztugay, E., Karatas, R., Jugreet, S., Mahomoodally, M.F., Boczkaj, G., 2022. Selectivity tuning by natural deep eutectic solvents (NADESs) for extraction of bioactive compounds from *Cytinus hypocistis* studies of antioxidative, enzyme-inhibitive properties and LC-MS profiles. Molecules 27. https://doi.org/10.3390/MOLECULES27185788.